EuroGNC
Madrid, Spain May 5th-7th 2026

Orbit Propagation Strategy for ST3LLARsat1 CubeSat Mission

Josep Peiro Pous Aerospace Engineering Department, Universidad Carlos III de Madrid (UC3M), Madrid, Spain

Andres Infante Adrian Aerospace Engineering Department, Universidad Carlos III de Madrid (UC3M), Madrid, Spain

Ghasem Sharifi Aerospace Engineering Department, Universidad Carlos III de Madrid (UC3M), Madrid, Spain

Behrad Vatankhahghadim Aerospace Engineering Department, Universidad Carlos III de Madrid (UC3M), Madrid, Spain

Andrés Marcos Aerospace Engineering Department, Universidad Carlos III de Madrid (UC3M), Madrid, Spain

ABSTRACT

ST3LLARsat-1 "BOIRA", the first student CubeSat at Universidad Carlos III de Madrid (UC3M), requires a robust onboard orbit determination (OD) capability for its Attitude Determination and Control System (ADCS). This article presents and validates a unified OD architecture centered on a single Simplified General Perturbations #4 (SGP4) propagator, comparing it against an initial dual-propagator (Numerical + SGP4) concept.

The system centers on a Pseudo-TLE Generation Algorithm that converts real-time GNSS data into standardized Two-Line Element (TLE) formats. By using a weighted Levenberg-Marquardt fit, the algorithm ensures that these "pseudo-TLEs" are mathematically precise. This dual-source approach allows the SGP4 propagator to remain highly accurate at all times: using live GNSS data when available, and automatically falling back to traditional ground-based TLEs if the signal is lost.

Using the full Space-Track catalog (31,753 objects), the algorithm reconstructs TLEs with epoch position errors in the $[10^{-7}, 10^{-6}]$ m bin for 99.94% of cases. In Initial Orbit Determination (IOD) test scenarios using simulated telemetry, a 24-hour data arc allowed for precise drag (B^*) estimation. This reduced the 24-hour prediction error to 0.01 km (10 m), whereas a 3-hour arc resulted in a 10.92 km error.

Finally, Model-in-the-Loop (MIL) simulations were conducted to compare both approaches. Under nominal operations, the system received simulated continuous 1 Hz GNSS updates over a 1-hour arc. Under these conditions, both solutions were essentially coincident: the unified SGP4 architecture achieved a Root Mean Square (RMS) algorithmic step error of 5.3275×10^{-6} km ($\approx$ 5 mm) versus 3.4045×10^{-8} km ($\approx$ 0.03 mm) for the numerical propagator. In a 3-day contingency scenario with daily GNSS updates—where actual propagation drift dominates—the SGP4 system proved more robust, exhibiting slower error growth than the numerical integrator.

1 Introduction

The ST3LLARsat1 mission, referred to as "BOIRA" (meaning "fog" in Catalan and Galician), is the first student CubeSat developed by the Universidad Carlos III de Madrid (UC3M). A comprehensive overview of the mission's architecture and analysis is detailed in previous work [1, 2]. Conceived as a 2U CubeSat—a standardized nanosatellite form factor measuring approximately $10 \times 10 \times 20$ cm—the project was selected in December 2022 by the European Space Agency (ESA) for participation in the *Fly Your Satellite!* (FYS!) Design Booster program, a 1.5-year program aimed at consolidating CubeSat designs. The mission wants to demonstrate advanced orbit determination and attitude control techniques on a CubeSat platform; therefore, precise knowledge of the spacecraft's position and velocity will be essential for maintaining telecommunications links and for attitude determination tasks, especially when reliance on onboard global navigation satellite system (GNSS) receivers is constrained by low sampling frequency or potential sensor failures [3].

To provide redundancy and autonomy, BOIRA's architecture combines GNSS measurements with a semi-analytical orbit propagation algorithm and Two-Line Element (TLE) data uplinked from the ground. The novelty presented in this work is a pseudo-TLE generation algorithm that reconstructs Brouwer-mean orbital elements directly from GNSS state vectors, in a procedure inspired by previous work from Vallado [4]. By feeding these pseudo-TLEs into the Simplified General Perturbations model (SGP4), it is potentially possible to remove the need for an onboard numerical propagator and achieve accurate, computationally lightweight orbit determination.

Modern orbit propagation for low-Earth-orbit satellites builds upon a long history of analytical and semi-analytical theory. Brouwer's solution of the J_2-perturbed two-body problem provided the first complete analytic description of satellite motion [5]. To support catalog propagation, Hoots and Roehrich developed the Simplified General Perturbations (SGP4) model for near-Earth objects and its deep-space counterpart, the Simplified Deep-space Perturbations (SDP4) model, introducing the TLE format to distribute mean orbital elements [6]. TLEs encapsulate the secular and long-period components of the orbit; the SGP4 propagator reconstructs short-period variations and applies a simplified atmospheric drag model parameterised by the ballistic coefficient B^*. Vallado and co-workers [7] rederived the algorithm and released a reference implementation, which corrected numerical and algorithmic shortcomings of the original *Space-Track Report #3* code by Hoots and Roehrich [6], and improved consistency across platforms. An important aspect almost always mentioned in literature is that, because TLEs are tied to the underlying analytical theory, they must be propagated with SGP4 and using them with different models can introduce significant errors.

Despite its well-known efficiency, SGP4 makes several approximations, such as the truncation of the gravity field to J_2–J_4 and the use of a simple exponential atmosphere, leading to position errors that can exceed 15 km for CubeSats with high area-to-mass ratios and variable frontal areas[3]. Furthermore, TLEs distributed on Space-Track can be 8–12 h old, and the prediction error grows roughly with time$^{1.5}$ after epoch [7]. After decades of using the SGP4, the U.S. Space Force released SGP4-XP, which augments SGP4 with EGM-96 gravity including J_5, the Jacchia-70 atmosphere model with solar flux indices, improved third-body and solar radiation pressure modelling, and resonance terms [8]. Conkey and Zielinski observed improved position accuracy for medium- and high-altitude orbits, but adoption is limited because XP TLEs, known as "type-4 TLEs", are not publicly available in a catalogue [9].

Many researchers have proposed orbit determination methods that treat successive TLEs as pseudo-observations. Levit and Marshall used batch least-squares to fit a high-fidelity numerical propagator to states derived from TLEs, obtaining range errors that increased by only 100 m per day [10]. Bennett [3] extended this approach with bias estimation, demonstrating that along-track biases for the satellites Stella and Starlette could be reduced by 64–74% after a 7-day propagation. Chen and Lin [11] analysed Starlink TLEs and found that using 10-day windows to build pseudo-observations improved five-day predictions by a factor of two, and that producing two pseudo-observations per orbit yielded a further 10% improvement.

Liu [12] proposed a simplex-based Monte Carlo technique to fit TLE-derived states, while Gunther [13] showed that adjusting TLE parameters using Doppler shifts observed at multiple ground stations and frequencies can reduce stale-TLE errors and enable near-real-time orbit maintenance.

In addition, the growth of small-satellite constellations has spurred interest in data-driven corrections to analytical propagators. Li [14] trained long short-term memory networks to predict drag coefficients from space-weather indices and improved low-Earth orbit predictions, whereas Rahman [15] used machine learning to correct SGP4 position and velocity errors for conjunction assessment. Acciarini [16] recently recast the propagator as a “differentiable SGP4 ($\partial SGP4$), enabling gradient-based optimisation and hybrid learning frameworks. This is made possible because dSGP4 allows for automatic differentiation, meaning machine learning algorithms can calculate exact gradients and backpropagate errors directly through the orbital physics model. These developments suggest a path toward high-fidelity propagation with low computational cost, which is currently a focus of research.

Based on the above, a unified orbit propagation architecture is proposed for ST3LLARsat1 that aims to combine the efficiency and ubiquity of SGP4 with accurate GNSS-derived pseudo-TLEs. Such pseudo-TLEs can then be fed into the propagator allowing for high-rate propagation without switching between different models, thereby maintaining consistency and reducing risk. Section 2 and 3 provide details of the pseudo-TLE algorithm and its implementation in ST3LLARsat-1, while Section 4 presents simulation results and on-board performance estimates.

2 Description of the mission

BOIRA’s primary objective is educational, providing UC3M students (mainly in its Master in Space Engineering, MISE) with hands-on experience in a real space project, with secondary objectives focused on technology demonstration and scientific exploration. Scientifically, the mission aims to validate the feasibility of measuring atmospheric water vapor using a Commercial Off-The-Shelf (COTS) spectrometer aboard a small spacecraft. Technologically, the mission seeks to demonstrate a compact, non-deployable antenna, and an on-board computer architecture designed to incorporate advanced Attitude Determination and Control Subsystem (ADCS) algorithms developed in-house [1].

Although the launch opportunity is yet to be finalized, mission analysis results by UC3M team [2] indicates the spacecraft must be injected into a Sun-Synchronous Orbit (SSO) with an altitude ranging from 415 km to 450 km, which correspond to Low Earth Orbit (LEO) regime. This specific altitude range ensures compliance with the recent ESA’s Space Debris Mitigation requirements [17], which requires atmospheric re-entry within five years of launch.

2.1 The Attitude Determination and Control Subsystem (ADCS)

As part of the advanced ADCS development objective, one of the sub-objectives is to demonstrate a robust, autonomous onboard orbit-determination (OD) capability. This is critical for the ADCS, which depends on accurate position, velocity, and time (PVT) estimates as essential inputs for reliable attitude control. This article will analyze and compare two potential architectures for achieving this goal, with a focus on presenting a streamlined approach.

2.1.1 Approach 1: Initial Dual-Propagator Concept

The initial architecture considered for the BOIRA mission—illustrated in Fig. 1a—follows a common dual-propagator pattern in the small-satellite literature. This baseline approach was originally chosen for its conceptual simplicity: it numerically integrates the equations of motion between GNSS measurements to obtain osculating elements, utilizing an SGP4/TLE propagator solely as a robust fallback during prolonged GNSS signal loss.

Specifically, the primary numerical propagator relies on Cowell's method to integrate the perturbed equations of motion. To maintain low computational overhead, the force model is restricted to Earth's central gravity and the J_2 perturbation, advanced via a fixed-step Runge-Kutta 4 (RK4) scheme ($\Delta t = 0.1$ s). In this baseline implementation, a direct-update strategy is employed; the state vector is strictly overwritten whenever a new GNSS measurement is received, without the use of an Extended or Unscented Kalman Filter (EKF/UKF).

While straightforward to implement, this unfiltered approach presents significant reliability challenges. GNSS receiver errors are complex and not straightforward to model accurately, making a direct-update mechanism inherently vulnerable when faced with noisy data or sensor glitches. Furthermore, maintaining two distinct propagation chains increases onboard software complexity. By contrast, the unified architecture presented in this work (Section 2.1.2) is computationally more efficient and provides built-in noise filtering via robust least-squares estimation.

2.1.2 Approach 2: Unified SGP4 Architecture

The primary objective of this work is to present and validate a streamlined, autonomous OD architecture developed for BOIRA. This unified system relies on a single SGP4 propagator driven by a newly developed Pseudo-TLE generation algorithm, which directly converts onboard GNSS telemetry into TLE-formatted orbital elements ("pseudo-TLEs").

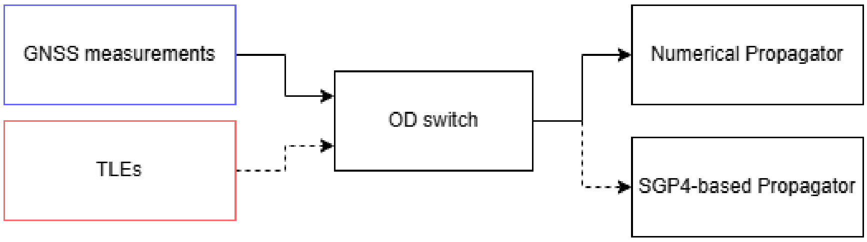

(a) Dual-Propagator concept

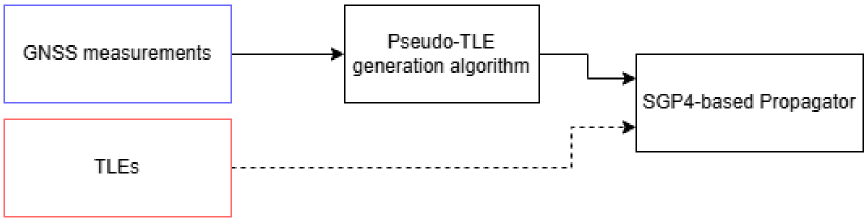

(b) Unified SGP4 Architecture

Fig. 1 OD Architecture Alternatives for BOIRA Mission

This unified approach, depicted in Fig. 1b, removes the need for a separate numerical propagator and the OD switch. The single SGP4 propagator will be continuously fed with the best available data: high-frequency, high-accuracy pseudo-TLEs when GNSS is active, and ground-uplinked TLEs as a fallback if GNSS is unavailable, which will prevent the generation of pseudo-TLEs. This article aims to demonstrate that this computationally lighter, unified system can meet the mission's accuracy and reliability requirements, offering a more efficient and autonomous solution for CubeSat orbit determination.

3 Pseudo-TLE Generation Algorithm

This section describes the algorithm that reconstructs a Brouwer-type mean element set, consistent with SGP4/SDP4, directly from TEME measurements, which in the case under study will be provided by the GNSS receiver. The method comprises: (i) SGP4 model and conventions, (ii) osculating-to-mean conversion to obtain a seed TLE from one or more ECI states, and (iii) a robust, weighted Levenberg-Marquardt (LM) fit of the mean elements (and optionally B^*) using TEME measurements.

3.1 SGP4 Model and Conventions

In the present work, Vallado's unified SGP4/SDP4 formulation is adopted [7]. SGP4 evolves Brouwer mean elements rather than instantaneous (osculating) elements. Unlike osculating elements, which capture the exact instantaneous trajectory including high-frequency perturbations, Brouwer mean elements have the short-period zonal contributions (primarily J_2 oblateness effects) analytically averaged out. This allows the model to integrate primarily the secular and long-period dynamics, which significantly improves computational efficiency.

Aerodynamic drag is represented by the dimensionless ballistic parameter B^*, which produces secular changes in the mean motion n and, consequently, in the semi-major axis a for near-Earth orbits. Let the TLE-style state vector m be defined as:

$$m = \{t_0, B^*, e, i, \Omega, \omega, M, n\} \tag{1}$$

where:

- t_0 is the epoch of the element set (typically expressed as a Julian Date).
- B^* is the B-star drag term.
- e is the mean eccentricity.
- i is the mean inclination.
- Ω is the mean Right Ascension of the Ascending Node (RAAN).
- ω is the mean argument of perigee.
- M is the mean anomaly.
- n is the mean motion, strictly reported in revolutions per day.

Mathematically, the SGP4 algorithm acts as a non-linear mapping function, denoted in this work as $\mathcal{P}$. It transforms the initial mean state vector m and a time-since-epoch Δt (in minutes) into an instantaneous, osculating Cartesian state vector. During this propagation, the algorithm "re-injects" the short-period perturbations that were previously averaged out. The mapping is expressed as:

$$[\mathbf{r}_{\text{TEME}}(t), \mathbf{v}_{\text{TEME}}(t)] = \mathcal{P}(m, \Delta t) \tag{2}$$

where $\mathbf{r}_{\text{TEME}}$ and $\mathbf{v}_{\text{TEME}}$ represent the osculating position and velocity vectors, respectively, expressed in the True Equator Mean Equinox (TEME) reference frame at time $t = t_0 + \Delta t$.

3.2 Osculating–to–Mean Conversion (Seed Generation)

Given an epoch TEME state $(\mathbf{r}, \mathbf{v})$, a non-singular osculating set O_{osc}^{ns} is formed to avoid angular degeneracies—mathematical singularities that occur in classical Keplerian elements when orbits are nearly circular (making the argument of perigee undefined) or nearly equatorial (making the ascending node undefined)—as recommended in the literature, e.g., [18–21]. This set is expressed as follows:

$$O_{\text{osc}}^{\text{ns}} = \{a,\ u,\ e_x,\ e_y,\ i,\ \Omega\}, \qquad u = \omega + M, \quad e_x = e\cos\omega, \quad e_y = e\sin\omega,$$

Classical orbital parameters are then obtained using:

$$e = \sqrt{e_x^2 + e_y^2}, \tag{3}$$

$$\omega = \operatorname{atan2}(e_y, e_x), \tag{4}$$

$$M = (u - \omega) \bmod 2\pi. \tag{5}$$

To obtain a seed consistent with the TLE dynamics, the osculating set is then mapped to the *Brouwer-type mean* elements advanced by SGP4 [5]. Concretely, the dominant short-period zonal contributions (principally the J_2 terms) are removed from the osculating a and n using the same compact correction used in SGP4's initialization: a J_2-dependent adjustment produces a mean semimajor axis a_{mean} and a corresponding mean motion n (reported in rev/day), while the angular variables are carried forward and regularized as described below. This step ensures that the seed is expressed in the same element convention that the propagator evolves.

As mentioned, angular variable regularization is performed according to the particular orbital regime to avoid singular behavior. Geometrically, "absorbing" an angle means bypassing an undefined reference point (like the perigee or the ascending node) and measuring the satellite's position or orientation from a more stable, well-defined reference direction. This is implemented as follows:

(i) **Nearly circular, inclined ($e \approx 0$):** The perigee becomes ill-defined, making both ω and M unstable. To resolve this, the argument of perigee is absorbed into the mean anomaly ($\omega \leftarrow 0$, $M \leftarrow (M + \omega) \pmod{2\pi}$). Geometrically, this creates a composite angle (the mean argument of latitude) that measures the satellite's position directly from the well-defined ascending node, completely bypassing the ambiguous perigee.

(ii) **Nearly equatorial, noncircular ($i \approx 0$):** The ascending node becomes undefined, destabilizing Ω and ω. Here, the RAAN is absorbed into the argument of perigee ($\Omega \leftarrow 0$, $\omega \leftarrow (\Omega + \omega) \pmod{2\pi}$). Geometrically, this defines the "longitude of perigee," meaning the perigee's location is measured directly from the vernal equinox rather than from the non-existent ascending node.

(iii) **Nearly circular and nearly equatorial ($e \approx 0$, $i \approx 0$):** Both the perigee and the ascending node are undefined. The triplet (Ω, ω, M) is replaced entirely by the mean longitude L, defined in Eq. (6), as the new reference angle:

$$L = \Omega + \omega + M \tag{6}$$

Geometrically, L represents the angle from the vernal equinox directly to the satellite, bypassing both ambiguous intermediate reference points.

This produces a mean-consistent seed $\mathbf{m}_0$ at the measurement epoch. In case only one epoch is available, B^* is initialized from an external estimate or a conservative default.

3.3 Robust weighted least–squares fit of the mean state

This stage turns the previously obtained seed into a *pseudo-TLE at the fixed epoch* that best reproduces the multi-epoch TEME arc under the SGP4 model. The epoch is held fixed: the mean elements (and optionally the drag term) are adjusted so that propagation from the epoch to each t_k matches the measurements.

The objective is to solve for a bounded, nonsingular parameterization

$$\mathbf{p} = [a,\ e_x,\ e_y,\ i,\ \Omega,\ L,\ z], \qquad B^* = b_{\max} \tanh z,$$

where (e_x, e_y) are the in-plane components of the eccentricity vector and L is the mean longitude, given by Eqs. (3) and (6), respectively. The tanh mapping limits $B^* \in [-b_{max}, b_{max}]$ while maintaining an unconstrained solve variable $z \in \mathbb{R}$, which prevents unbounded drag estimates without introducing hard box constraints [22]. Here, b_{max} is a predefined empirical constant representing the maximum physically plausible drag value ($b_{max} = 0.01$ in the case under study), chosen to prevent numerical divergence in the presence of noisy measurement blocks.[1]

At each measurement epoch t_k (minutes since the fixed epoch), the propagator built from the current $\mathbf{p}$ produces a predicted TEME state $(\hat{\mathbf{r}}_k, \hat{\mathbf{v}}_k)$. With the measurement $(\mathbf{r}_k, \mathbf{v}_k)$, the residual block is formed following the form suggested in Vallado [4]:

$$\mathbf{e}_k = \begin{bmatrix} (\mathbf{r}_k - \hat{\mathbf{r}}_k)/\sigma_r \\ (\mathbf{v}_k - \hat{\mathbf{v}}_k)/\sigma_v \end{bmatrix}, \qquad s_k = \sqrt{\frac{1}{m_k}\sum_{i=1}^{m_k} e_{k,i}^2}, \quad m_k \in \{3, 6\},$$

where σ_r and σ_v are the assumed 1σ errors for position [km] and velocity [km/s], and m_k is the block dimension (3 when only position is used and 6 when velocity is introduced). The scalar s_k is the block RMS in sigma units, which measures how "large" the error of the epoch is relative to the noise model.

Two simple weights are applied to each block before stacking the residuals, which are gathered in Eq. (7).

The first weight (w_k) limits the influence of atypical epoch blocks, such as poor GNSS fixes or sensor glitches [23, 24], by applying a piecewise Huber-type loss function. Unlike standard least-squares, where squared errors from extreme outliers can disproportionately skew the calculated orbit, a Huber formulation treats nominal errors quadratically while applying a linear penalty to extreme outliers. Consequently, well-explained measurement blocks ($s_k \le c$) retain full weight ($w_k = 1$), whereas highly anomalous blocks are smoothly down-weighted proportionally to c/s_k. The tuning parameter c defines the sigma-unit threshold for this transition. In this implementation, the threshold is set to $c = 1.345$; as demonstrated by Holland and Welsch [25], since this specific constant yields exactly 95% asymptotic statistical efficiency under Gaussian error distributions, what balances nominal precision with robust outlier rejection.

The second (g_k) gives the later samples a modest extra weight to help identify slow secular effects (drag) over a short arc, with $T_{\text{ref}} > 0$ being a time scale (minutes) and $p \ge 0$ a small exponent. Choosing $p \in [0, 1]$ and T_{ref} comparable to the arc length leads to a gentle, monotone emphasis; setting p=0 or $T_{\text{ref}} \to \infty$ recovers $g_k \equiv 1$, which implies no temporal emphasis.

$$w_k = \begin{cases} 1, & s_k \le c, \\ \dfrac{c}{s_k}, & s_k > c, \end{cases} \qquad g_k = 1 + \left(\frac{|t_k|}{T_{\text{ref}}}\right)^p \tag{7}$$

When short-arc drag is effectively unobservable (e.g., very long period or high eccentricity), the drag variable is held fixed (z constant) and the extra weights are neutralized ($w_k \equiv 1$, $g_k \equiv 1$), leading to a stable geometry-only refinement of $(a, e_x, e_y, i, \Omega, L)$. The same setting is enforced when a pseudo-TLE is derived from a single TEME state (no time span), as drag and other slow secular effects cannot be obtained from one instant.

Let $\mathbf{r}$ be the long vector obtained by stacking the weighted blocks $\sqrt{w_k}\, g_k\, \mathbf{e}_k$. Therefore, the quantity minimized at each iteration is $J(\mathbf{p})$:

$$J(\mathbf{p}) = \frac{1}{2}\,\|\mathbf{r}\|_2^2 \tag{8}$$

---

[1] Here tanh acts as a squashing function [22]: near z=0 the derivative $b_{\text{max}}\text{sech}^2 z$ is almost constant (well-conditioned), while for large $|z|$ the map saturates, limiting the influence of extreme updates to B^*.

A finite-difference Jacobian $\mathbf{A} = \partial(\sqrt{w g}\,\mathbf{e})/\partial\mathbf{p}$ is assembled by perturbing one parameter at a time and re-propagating to all t_k; perturbations are retried with smaller steps if any trial state is invalid.[2] Aiming to improve conditioning, columns of the Jacobian are scaled with the diagonal matrix $\mathbf{S}$, defined in Eq. (9) as follows:

$$\mathbf{S} = \mathrm{diag}\big(1/\|\mathbf{A}(:,1)\|_2, \ldots, 1/\|\mathbf{A}(:,n)\|_2\big), \quad \mathbf{A}_s = \mathbf{A}\,\mathbf{S} \tag{9}$$

Therefore, the damped least-squares update is computed with Eq. (10), with $\lambda > 0$ reduced on successful steps (more aggressive) and increased on rejected steps (more cautious).

$$\big(\mathbf{A}_s^\top\mathbf{A}_s + \lambda\,\mathbf{I}\big)\,\mathbf{y} = \mathbf{A}_s^\top\mathbf{r}, \qquad \Delta\mathbf{p} = \mathbf{S}\,\mathbf{y} \tag{10}$$

In each step, the proposed mathematical update must first pass a physical validity check to ensure the orbital elements represent a realistic, Earth-bound trajectory. Because the unconstrained solver might attempt mathematically optimal but physically impossible updates, the algorithm explicitly verifies that the orbit remains closed (eccentricity $e < 1$), the semi-major axis is strictly positive ($a > 0$), and the perigee radius remains safely above the Earth's surface ($a(1-e) > R_\oplus$). If the proposed state is physically valid, the step is accepted provided the overall cost decreases ($J(p + \Delta p) \leq J(p)$) [18]; otherwise, the step is rejected and the damping parameter λ is enlarged to force a smaller, more conservative update. The process stops when the scaled step is small ($\|\mathbf{y}\|_\infty$ below tolerance) or the residual RMS ceases to improve.

On convergence, classical angles are recovered from (e_x, e_y, L) as indicated in Eqs.(3)-(6), and the mean motion is reported as $n = \frac{86400}{2\pi}\sqrt{\mu/a^3}$ in revolutions per day. The result is a TLE-compatible vector at the original epoch that reproduces the measured arc under SGP4. The robust weighting protects the pseudo-TLE from occasional bad measurements. Furthermore, because the physical effects of atmospheric drag build up very slowly and are difficult to detect over short observation windows, the algorithm applies a time-based weight (g_k). By assigning slightly more mathematical importance to the measurements at the end of the arc, the solver is forced to account for the accumulated along-track delay caused by drag. Finally, the bounded drag parameter prevents unphysical solutions, leading to reliable pseudo-TLE generation. For the sake of illustration, a flowchart explaining the algorithm is included in Appendix A.

4 Simulation and Results

This section evaluates the performance and robustness of the proposed Pseudo-TLE Generation Algorithm through three distinct test scenarios. First, Section 4.1 verifies the algorithm's core mathematical accuracy by reconstructing TLEs for the entire active Space-Track catalog using single-epoch states. Next, Section 4.2 applies the algorithm to a simulated Initial Orbit Determination (IOD) scenario representative of the BOIRA mission, highlighting the impact of observation arc length (3-hour versus 24-hour) on drag estimation and subsequent predictive accuracy. Finally, Section 4.3 addresses the operational challenge of telemetry latency by applying the algorithm to the "Delayed TLE" problem, utilizing Vallado's "tough cases" [4] to demonstrate stable re-epoching across various orbital regimes.

---

[2] During the finite-difference Jacobian computation, parameter perturbations are retried with smaller step sizes if any trial state becomes physically invalid. Validity is assessed by ensuring the perturbed elements remain strictly finite, represent a bound, closed elliptical orbit (eccentricity $0 \leq e < 1$), and that the semi-major axis remains within operationally feasible bounds ($6378 < a < 50000$ km).

4.1 Verification: Full Catalog Testing

To evaluate the algorithm's ability to reconstruct a TLE from a single TEME state, a verification campaign over the entire Space-Track catalog [26] has been run, totaling 31,753 non-decayed objects.[3] For each object, SGP4 at the TLE epoch ($\Delta t = 0$) is evaluated to obtain a reference TEME position–velocity state, then the procedure in Sec. 3 is applied to reconstruct a TLE from that state. Finally, a comparison of the reconstructed TLE to the original is made by measuring the epoch position error in TEME.

As can be observed in Table 1 (left), this leads to a median absolute element differences close to numerical zero, which holds when analysed in the state space ($|\Delta r|$, $|\Delta v|$). The table on the right gathers the bin ranges and the amount of samples falling in each of them, which is graphically depicted in the log-decade histogram of $\|\Delta \mathbf{r}\|$ at the epoch, represented in Fig. 2. The plot is found to be sharply left-skewed, with 99.94% (31,734/31,753) test cases falling in the $[10^{-7}, 10^{-6})$ m bin. When adding the results of the first three bins, it is observed that at least 99.98% are < 1 mm, with only 7 cases exceeding 1 mm, and a single case that is in the centimeter decade (max = 1.81×10^{-2} m).

Median absolute differences		
Inclination	$\lvert\Delta i\rvert$	0 deg
RAAN	$\lvert\Delta\Omega\rvert$	0 deg
Argument of perigee	$\lvert\Delta\omega\rvert$	4.206×10^{-12} deg
Mean anomaly	$\lvert\Delta M\rvert$	4.178×10^{-12} deg
Mean motion	$\lvert\Delta n\rvert$	5.329×10^{-15} rev/day
Radial position component	$\lvert\Delta r\rvert$	9.142×10^{-13} km
Velocity magnitude	$\lvert\Delta v\rvert$	1.110×10^{-15} km/s

Epoch position-error bins		
Range [m]	Percent	Count
$[10^{-7}, 10^{-6})$	99.94%	31734
$[10^{-6}, 10^{-5})$	0.003%	1
$[10^{-5}, 10^{-4})$	0.003%	1
$[10^{-4}, 10^{-3})$	0.031%	10
$[10^{-3}, 10^{-2})$	0.019%	6
$[10^{-2}, 10^{-1})$	0.003%	1

Table 1 Epoch ($\Delta t = 0$) reconstruction over the full catalog ($N = 31{,}753$). Left: median absolute differences. Right: histogram of epoch position error $\|\Delta \mathbf{r}\|$ (TEME); only nonzero bins shown.

$$\text{Min} = 10^{-7}\ \text{m},\ \ \text{Median} = 10^{-7}\ \text{m},\ \ \text{Max} = 1.81 \times 10^{-2}\ \text{m}.$$

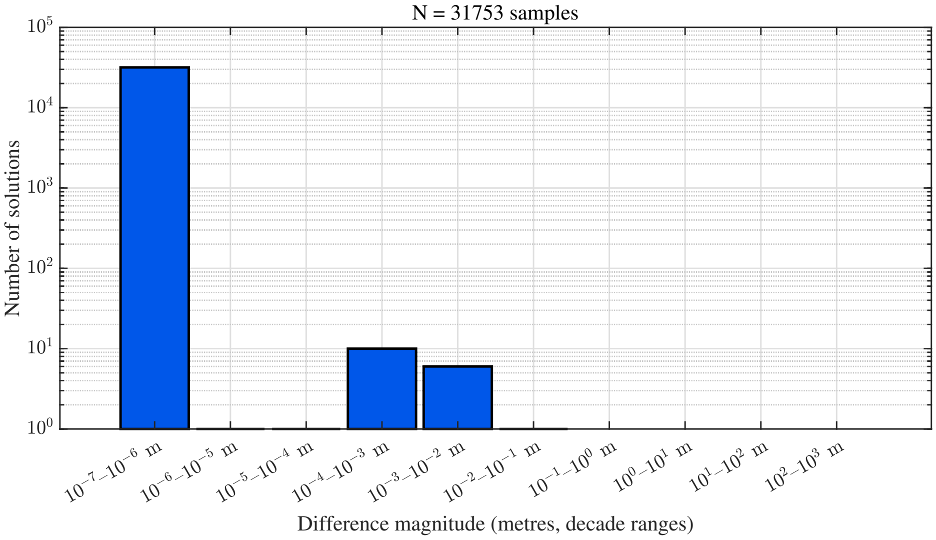

Fig. 2 Epoch position-error magnitude between the original TLE and the TLE reconstructed from its SGP4 TEME state ($\Delta t = 0$), for N = 31,753 catalog objects. Histogram uses decade bins in meters. Median = 10^{-7} m.

---

[3] The value 31,753 corresponds to the number of non-decayed objects in Space-Track catalog as of October 2025.

Fig. 3 shows the epoch position-difference versus apogee (left) and perigee (right), coloured by orbit regime as defined by Vallado [18]. The different shapes make clear that the outliers in Table 1 concentrate in two families: *deep-space* trajectories (GEO and supersynchronous; upward-pointing triangle), which appear at very high apogee ($\gtrsim 3 \times 10^4$ km) where SGP4 uses the deep-space model (SDP4) and the mean-element to TEME state mapping is more sensitive with weak B^* observability; and the *high-eccentricity/low-perigee* orbits (diamond), which are located near perigee ≈ 0 km where local nonlinearities amplify small numerical differences. In contrast, *LEO* and *MEO* objects (circle and square) have error close to zero for all altitudes, confirming the histogram's conclusion that the TLE reconstruction is essentially exact for nominal regimes. Overall, there is no systematic growth of error with altitude, as the small right tail is localized to the deep-space and high-e/low-perigee regimes identified by Vallado's classification [18].

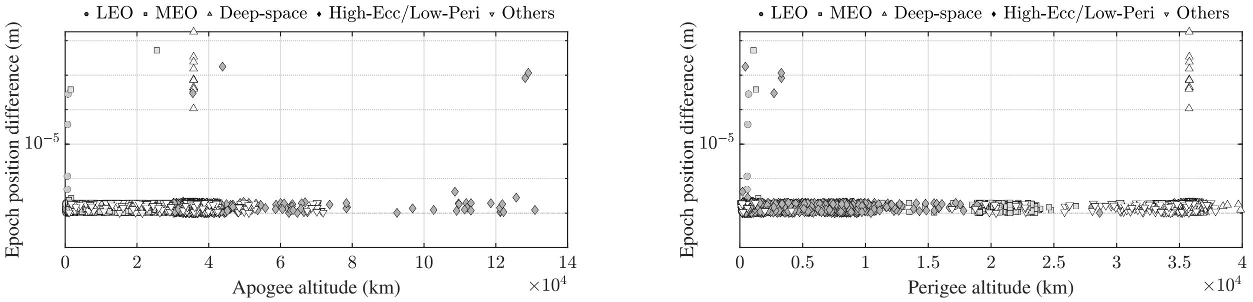

(a) Error vs. apogee altitude. **(b) Error vs. perigee altitude.**

Fig. 3 Epoch position difference (log scale on y) as a function of apogee/perigee altitude.

4.2 Application to the Initial Orbit Determination (IOD) Problem

This section validates the pseudo-TLE generation algorithm in a practical scenario: the Initial Orbit Determination (IOD) problem for a LEO satellite, representative of the BOIRA mission, owing to the studies conducted by UC3M team [2].

4.2.1 Test Scenario and Methodology

To simulate an operational environment, a high-fidelity "ground truth" ephemeris was used as the basis for the test. This ephemeris, containing a 7-day trajectory of the satellite, was generated using a high-precision numerical integrator within STK, which accounts for a comprehensive force model, including high-order geopotential terms, atmospheric drag, third-body gravity, and solar radiation pressure.

Parameter	**Value**
Epoch (UTC)	2024-01-01 12:00:00.0
Semi-major Axis	6921 km
Eccentricity	0.0
Inclination	98.6°
RAAN	280.0°
Argument of Perigee	0.0°
Mean Anomaly	0.0°

Table 2 "Ground Truth" Orbit Data for the IOD Test Scenario

From the data harvested from this propagator, two distinct test cases were created to evaluate the algorithm's performance under different conditions:

1) **A 3-hour short-arc scenario**, representing a challenging IOD case where a rapid orbital solution is required from limited data.
2) **A 24-hour long-arc scenario**, used for comparative analysis to demonstrate the effect of observation arc length on orbit determination accuracy.

For both scenarios, the high-fidelity ECI (J2000) data was downsampled to a 60-second interval and converted to the TEME frame required by the SGP4 propagator. To simulate the output of the GNSS receiver selected for the BOIRA mission (Orion B16 GNSS), zero-mean Gaussian noise was added to the clean TEME state vectors, with standard deviations of $\sigma_r = 10\,\mathrm{m}$ for position and $\sigma_v = 0.01\,\mathrm{m\,s^{-1}}$ for velocity, consistent with the performance of the receiver [27]. Furthermore, to explicitly test the robustness of the fitter, two significant 5σ outliers were injected into each measurement arc at arbitrary times.

It is important to note that, instead of comparing the final fitted TLE directly against the high-fidelity ground truth, the comparison is made against a *benchmark TLE* generated from the *clean*, downsampled data arc. This approach allows isolating the performance of the robust fitting algorithm, since any direct comparison to the high-fidelity ephemeris would combine two distinct error sources: 1) the algorithm's error in handling noisy and outlier-corrupted data, and 2) the inherent model mismatch error between the simplified SGP4 propagator and the complex dynamics of the real world.

4.2.2 Performance Analysis and Orbit Prediction Accuracy

The results from the 3-hour IOD scenario confirm the algorithm's robustness, as the fitter converged to a stable solution despite the presence of significant outliers. The in-arc Root Mean Square (RMS) position error, calculated by comparing the propagated TLE with the clean truth data over the 3-hour arc, was only 81 m (see Table 3), which indicates that the algorithm successfully filtered the noise and treated the outliers to produce a high-fidelity representation of the true trajectory over the observation window.

The ultimate measure of an IOD solution, however, is its predictive accuracy. The TLE generated from the 3-hour noisy data arc produced a total position error of 10.92 km after 24 hours of propagation, when compared to the benchmark TLE obtained with clean orbit data. This performance is consistent with real-world TLE accuracy for CubeSats, where 24-hour prediction errors of 10–30 km are common for TLEs generated from limited tracking data [28]. The error is attributed to the low observability of atmospheric drag over a short arc, since the fitter estimated a B^* value of 3.49×10^{-3}, which departs from the 5.15×10^{-4} derived from the clean benchmark data (see Table 3). This error in B^* is the principal driver of the large, accelerating in-track prediction error, as visualized in Fig. 4.

To quantify this impact of observation arc length on prediction accuracy, the test was repeated using a 24-hour data arc. The results, contrasted with the 3-hour scenario in Table 3 and Fig. 4, clearly demonstrate the significant effect of arc length on predictive power. In contrast to the short arc, the 24-hour arc spans over 15 orbital periods, allowing the secular trend of drag-induced orbital decay to become a strong, unambiguous effect. This enables the fitter to estimate the B^* parameter with extremely high precision. For the 24-hour fit, the estimated B^* of 4.9222×10^{-4} was nearly identical to the benchmark value of 5.1500×10^{-4}, virtually eliminating the source of secular error growth.

Parameter	3-Hour Arc (IOD Scenario)	24-Hour Arc (Long-Arc Fit)
Fit Quality		
In-Arc RMS Position Error	0.081 km	0.561 km
B^* (5.1500×10^{-4} for benchmark)	3.49×10^{-3}	4.9222×10^{-4}
Prediction Accuracy		
24-Hour Prediction Error	10.92 km	0.01 km

Table 3 Comparison of Orbit Determination Performance for Short (3-Hour) and Long (24-Hour) Observation Arcs

Consequently, the rapid secular error growth found for the 3-hour case is replaced by a small, oscillatory trend, reducing the 24-hour prediction error by three orders of magnitude to just 10 m, which can be explained by inherent, unmodeled short-period perturbations within the SGP4 model. This comparative analysis therefore confirms the algorithm's dual utility: it is effective for IOD from short arcs for initial acquisition, but its long-term prediction accuracy is substantially enhanced when longer data arcs are available, since it allows for a better computation of drag through B^* parameter estimation.

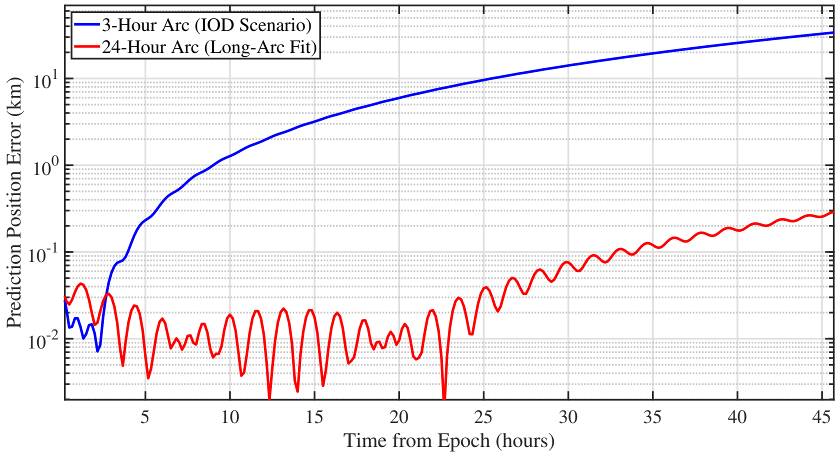

Fig. 4 Prediction error growth over a 48-hour period for TLEs generated from a 3-hour arc (blue) and a 24-hour arc (red). Error presented in log scale.

4.3 Application to the Delayed TLE Problem

In operations, the epoch of an uplinked TLE usually does not coincide with the onboard start time for propagation and when a known latency is present: $\Delta t_{\text{delay}} = t_{\text{onboard}} - t_{\text{TLE}}$. The procedure described in Sec. 3 is proposed as a way to tackle the problem, by taking the received TLE and *re-epoching* it so that it is valid at the onboard epoch. To that end, the original set is propagated by Δt_{delay} with SGP4 to t_{onboard}, and the resulting TEME state is converted back to mean elements via the pseudo-TLE generation algorithm, yielding a time-aligned "delayed TLE" suitable for subsequent onboard propagation.

The latter will be assessed by considering Vallado's "tough cases" [4], which correspond to particularly exotic orbital examples in Space-Track catalog [4]. For each case, the re-epoching will be applied and the result will be compared against the catalog TLE issued at the common epoch, calculating element-wise differences. In geostationary orbits (GEO), the nearly circular and nearly equatorial nature of the

---

[4] The TLEs used are harvested from the cited Vallado article, listed in *Appendix C – Test Case Listing* [4]

orbit causes the classical angles (Ω, ω, M) to become mathematically ill-conditioned. To ensure a stable and physically meaningful comparison, the analysis for GEO objects is performed using the GEO-safe mean longitude $\lambda = \Omega + \omega + M$ instead.

Table 4 collects the reconstruction statistics obtained with the re-epoching procedure of Sec. 3. In LEO and MEO, the method behaves as expected: element discrepancies remain at the micro–to–milli level and angular errors are small, in spite of the long delays considered (see $\overline{\Delta t}$ in the caption). These figures are consistent with small epoch state-space residuals $||\Delta \mathbf{r}||$, $||\Delta \mathbf{v}||$ and with the fact that any remaining difference could be explained by the secular effects in n (and, in LEO, by B^*). On the contrary, in GEO, large dispersions appear when classical angles are compared directly, and the sample also exhibits large spreads in $\Delta\lambda$, reflecting potential differences accumulated over long catalog latencies and the well-known ill-conditioning of (Ω, ω, M) near-circular, near-equatorial orbits. For HEO, the differences increase moderately due to the higher sensitivity of Ω and ω at a high eccentricity; however, $\Delta\lambda$ remains within a few degrees and the consistency of the mean movement is high.

(a) LEO (N=31; $\overline{\Delta t}$ = 580.47 min**)**

Metric	Mean	RMS	Max
B*	-9.204×10^{-6}	5.272×10^{-5}	1.672×10^{-4}
e	1.893×10^{-6}	7.649×10^{-6}	3.170×10^{-5}
i (°)	6.452×10^{-5}	3.520×10^{-4}	0.0018
Ω (°)	-1.217×10^{-4}	4.396×10^{-4}	0.001 83
ω (°)	0.4020	5.741	23.83
M (°)	−0.4049	5.737	23.82
n (rev/day)	-3.790×10^{-6}	5.263×10^{-5}	2.039×10^{-4}
$\Delta\lambda$ (°)	−0.003	0.011	0.042

(b) MEO (N=2; $\overline{\Delta t}$ = 701.73 min**)**

Metric	Mean	RMS	Max
B*	0	0	0
e	-5.150×10^{-7}	1.201×10^{-6}	1.600×10^{-6}
i (°)	-2.981×10^{-4}	2.981×10^{-4}	2.982×10^{-4}
Ω (°)	0.016	0.016 11	0.017 91
ω (°)	0.36	0.493	0.6968
M (°)	−0.3618	0.5037	0.7122
n (rev/day)	2.850×10^{-7}	4.031×10^{-7}	5.700×10^{-7}
$\Delta\lambda$ (°)	0.014	0.018	0.026

(c) GEO (N=7; $\overline{\Delta t}$ = 595.31 min**)**

Metric	Mean	RMS	Max
B*	0	0	0
e	1.675×10^{-5}	4.819×10^{-5}	1.274×10^{-4}
i (°)	0.004 126	0.011 48	0.030 30
Ω (°)	9.512	48.80	103.4
ω (°)	34.30	39.19	65.78
M (°)	53.43	130.4	209.9
n (rev/day)	6.710×10^{-5}	1.750×10^{-4}	4.629×10^{-4}
$\Delta\lambda$ (°)	45.812	124.834	172.311

(d) HEO (N=2; $\overline{\Delta t}$ = 1019.09 min**)**

Metric	Mean	RMS	Max
B*	0	0	0
e	3.876×10^{-6}	4.277×10^{-6}	5.684×10^{-6}
i (°)	9.518×10^{-4}	9.635×10^{-4}	0.001 102
Ω (°)	0.025 48	0.025 64	0.028 39
ω (°)	−0.1141	0.1150	0.1286
M (°)	−0.023 39	0.023 53	0.025 89
n (rev/day)	7.700×10^{-7}	8.228×10^{-7}	1.060×10^{-6}
$\Delta\lambda$ (°)	−0.112	0.113	0.126

Table 4 Delayed–TLE reconstruction errors by element and across orbital regimes (updated with the validation dataset). Overall average delay across all cases: $\overline{\Delta t}_{\text{all}}$ = 609.61 min **(N=42).**

It is important to mention that the latency in the TLE pairs in the catalog is high, which explains the departures found. In the analysis, cases with lapse between consecutive Space-Track TLEs exceeding one day (> 1440 min) were excluded because the delay is too large to be representative for onboard use. The regime counts (N)—shown in the subcaptions—reflect this filtering. Note in particular that the MEO and HEO samples are small, so their statistics should be interpreted accordingly.

5 Validation: Unified SGP4 vs. Baseline Numerical Propagator

With the aim of validating the unified SGP4 architecture, which will embed the algorithm developed, a model-in-the-loop (MIL) simulator in Matlab/Simulink has been used. The simulator's primary function is to generate a high-fidelity "ground truth" trajectory using the high-precision data described in the IOD scenario of Section 4.2. This validation framework is used to test and compare the two orbit determination architectures presented in Section 2.1: the unified SGP4 and the dual-propagator approach. The comparison is performed under two key operational scenarios: nominal operations, characterised by continuous availability of GNSS data, and contingency operations, which simulate extended signal loss periods. The baseline numerical simulator detailed in Section 2.1.1 is utilized as the benchmark to represent this initial dual-propagator concept.

To assess the approaches, two MIL simulations were conducted:

1) **Nominal operations (continuous GNSS data).** In this scenario, the pseudo-TLE generator is refreshed every 1 second (1 Hz), matching the high-frequency navigation solution expected in nominal BOIRA operations. A short 1-hour time span is propagated using both the unified SGP4 and numerical propagators for demonstration purposes.
2) **Contingency operations (extended GNSS signal loss).** To simulate a prolonged outage, GNSS measurements are provided only once per day. The unified SGP4 propagator therefore uses daily mean-element fits from its pseudo-TLE generator, while the numerical integrator runs freely without measurement correction. A three-day MIL simulation is set to observe how the reception of a new measurement once every day affects the resulting position prediction.

To ensure the reproducibility of the simulations, the Simulink environment was configured to use a variable-step `ode45` (Dormand-Prince) solver. To balance computational efficiency with the rigorous numerical precision required to capture both the short-period J_2 oscillations and the long-term secular drift, the solver was constrained with a maximum step size of 1 s, a relative error tolerance of 10^{-6}, and an absolute tolerance of 10^{-9}.

5.1 Nominal operations results

The one-hour simulation with continuous GNSS updates shows that the unified SGP4 and the numerical integrator deliver virtually coincident trajectories because each new measurement re-epochs the propagated state, leading to a reset in the error. With 1 Hz updates, the numerical propagator's one-step error remains extremely small in Approach 1, while the unified-SGP4 solution (Approach 2) is continually refreshed by pseudo-TLEs.

Quantitatively, the RMS position error over the hour is 5.3275×10^{-6} km ($\approx$ 5 mm) for the SGP4 solution and 3.4045×10^{-8} km ($\approx$ 0.03 mm) for the numerical integrator (Table 5). Component-wise SGP4 statistics in the local Radial, In-track, and Cross-track (RIC) coordinate frame (Table 6) show sub-millimetre biases (radial -4.57×10^{-7} km, in-track 2.96×10^{-7} km, cross-track 9.02×10^{-7} km) and centimetre-level dispersions (radial $\sigma = 1.60 \times 10^{-5}$ km, in-track $\sigma = 1.88 \times 10^{-5}$ km, cross-track $\sigma = 1.22 \times 10^{-4}$ km).

Fig. 5 exhibits a very small red ondulation for SGP4 at the 10^{-5} km scale, which can be explained by the combined effect of (i) repeatedly fitting *mean* elements to slightly noisy osculating GNSS PV at 1 Hz, and (ii) the mean$\leftrightarrow$osculating mapping and short-period corrections inherent to SGP4. The latter leads to changes in fitted mean motion/mean anomaly and in B^* inducing centimetre-level along-track errors that appear as a gentle undulation. Regarding the numerical curve, it presents the same trend, although two orders of magnitude smaller since it is re-initialized with osculating GNSS PV and uses the same high-fidelity force model as the truth for each 1-s step. Nevertheless, the assumption of noise-free GNSS in the numerical branch is optimistic and likely underestimates the operational error; with realistic measurement noise and filter gains, the post-update difference would be limited by the GNSS noise, narrowing the apparent gap between the numerical and SGP4 curves in this nominal regime. Overall, frequent updates prevent any secular divergence and keep both solutions within millimetre accuracy over the full hour.

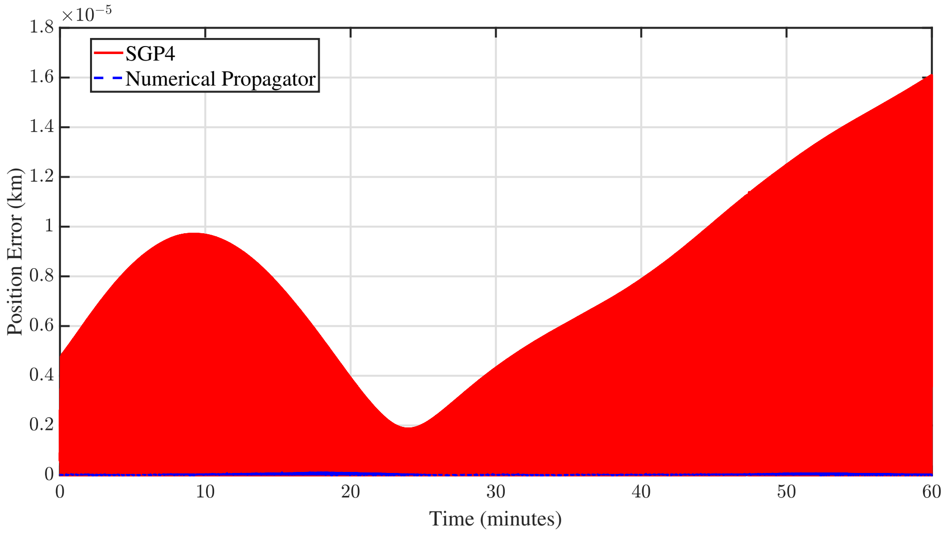

Fig. 5 Position error evolution during the nominal (1-hour) simulation with continuous GNSS updates.

5.2 Contingency operations results

When GNSS data are available only once per day, the differences between the propagators become more pronounced. Simulations of the baseline numerical integrator demonstrate that without continuous GNSS updates to overwrite the state, the uncalibrated J_2-only model drifts rapidly; the error grows to roughly 4.5 km after one day, and can reach up to 23 km after seven days.

For the SGP4, Vallado notes that for low-Earth orbits the error after two days is typically 4–5 km [7]. This slower growth found in the present case is because the pseudo-TLE generator averages out high-frequency variations, generating a more consistent representation of the true orbit. However, the B^* parameter is estimated at the epoch and remains fixed, so any error in B^* introduces a systematic in-track bias that grows over time (see Table 6). Conkey emphasises that in SGP4 the in-track error is generally the dominant term and can grow to tens of kilometres after a few days [9].

These effects are evident in the three-day MIL simulation. Table 5 shows that the RMS position error of the unified-SGP4 solution is about 3.91 km, whereas the numerical integrator exceeds 5 km. The error statistics in Table 6 indicate that the in-track component contributes most of the bias (2.87 km) and dispersion (2.64 km), consistent with the sensitivity of the mean motion to drag modelling. The radial and cross-track errors remain smaller, because the propagator is able to model gravitational perturbations well and these components are less sensitive to drag. Fig. 6 illustrates the error evolution: the numerical solution diverges steadily due to uncorrected modelling errors, while the SGP4 solution stays bounded but exhibits a systematic in-track drift.

Overall, the unified SGP4 architecture offers better robustness during prolonged GNSS outages by reducing short-period oscillations and limiting secular growth, though further refinement of the B^* estimation would be needed to minimise the remaining along-track bias.

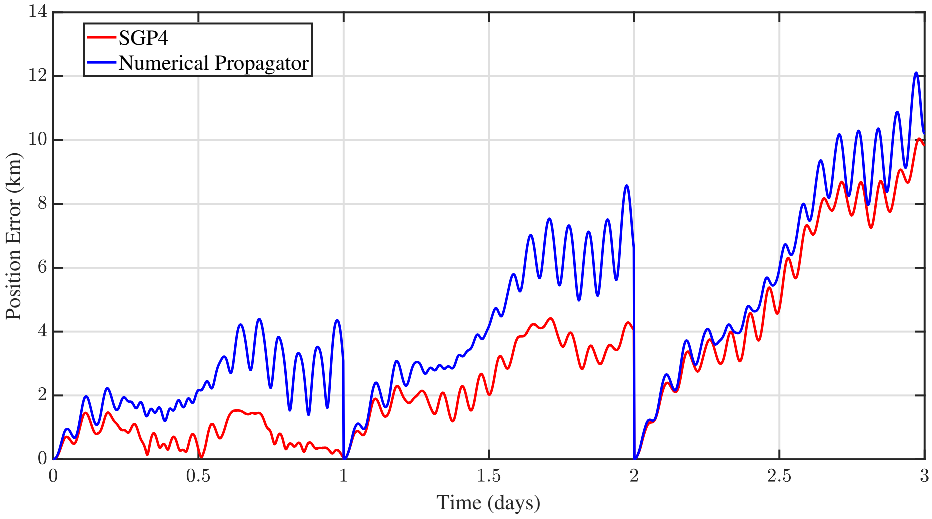

Fig. 6 Position error evolution during the contingency (3-day) simulation with daily GNSS updates.

Simulation	**SGP4**	**Numerical**
Sim 1 (1 hour, nominal)	5.3275×10^{-6}	3.4045×10^{-8}
Sim 2 (3 days, contingency)	3.9100	5.0959

Table 5 RMS position error (km) comparing SGP4 and the numerical propagator for the two simulations. Sim 1: 1 hour with continuous GNSS (1 Hz). Sim 2: 3 days with a daily GNSS update.

Metric	Sim 1: 1 hour (Nominal)	Sim 2: 3 days (Contingency)
Radial Component [km]		
Mean bias	-4.5699×10^{-7}	-3.7800×10^{-2}
Std. dev.	1.5990×10^{-5}	1.4300×10^{-1}
In-Track Component [km]		
Mean bias	2.9633×10^{-7}	2.8707
Std. dev.	1.8760×10^{-5}	2.6415
Cross-Track Component [km]		
Mean bias	9.0237×10^{-7}	-4.8000×10^{-3}
Std. dev.	1.2244×10^{-4}	2.1850×10^{-1}

Table 6 SGP4 position error statistics in the RIC frame for the nominal (1-hour) and contingency (3-day) simulations.

6 Conclusions

This work has proposed and validated a unified on-board orbit determination architecture for the ST3LLARsat1 mission that replaces the dual-propagator approach with a single SGP4-based propagator fed by a pseudo-TLE generation algorithm. By converting real-time GNSS measurements into Brouwer-mean elements via a robust Levenberg–Marquardt fit, the algorithm reconstructed TLEs for the 31,753-object Space-Track catalogue with sub-metre accuracy in 99.94% of cases. For initial orbit determination, extending the data arc from 3 to 24 hours reduced prediction errors from 10.92 km to just 10 m, underscoring the need for long arcs to accurately estimate drag.

Model-in-the-loop simulations of nominal operations (1 Hz GNSS over 1 hour) showed the unified architecture closely matches the numerical algorithm used in the dual-propagator approach, yielding a 5.3×10^{-6} km ($\approx$ 5 mm) RMS position error versus 3.4×10^{-8} km ($\approx$ 0.03 mm). This confirms that frequent updates effectively bound prediction errors. In a three-day contingency with daily GNSS updates, the unified-SGP4 solution proved more robust (3.91 km RMS error vs. 5.10 km for the numerical propagator), consistent with Vallado's observation that SGP4 position errors typically grow to 4–5 km after two days for low-Earth orbits [7], whereas numerical methods suffer greater along-track drift when left uncorrected. Although residual error is dominated by an in-track bias from imperfect ballistic parameter estimation—a known TLE limitation [9]—the radial and cross-track errors remain small, satisfying mission requirements.

The unified architecture meets ST3LLARsat1's navigation objectives with reduced computational load and software complexity, eliminating the need for an OD switch and a numerical propagator. It also ensures seamless transitions to ground-uplinked TLEs during GNSS outages. Future work should focus on improving the estimation of the ballistic parameter to further reduce the in-track bias.

Ultimately, the unified-SGP4 architecture provides a robust, efficient, and scalable solution for CubeSat orbit determination that can readily be applied to future small-satellite missions.

A Pseudo-TLE Generation Algorithm

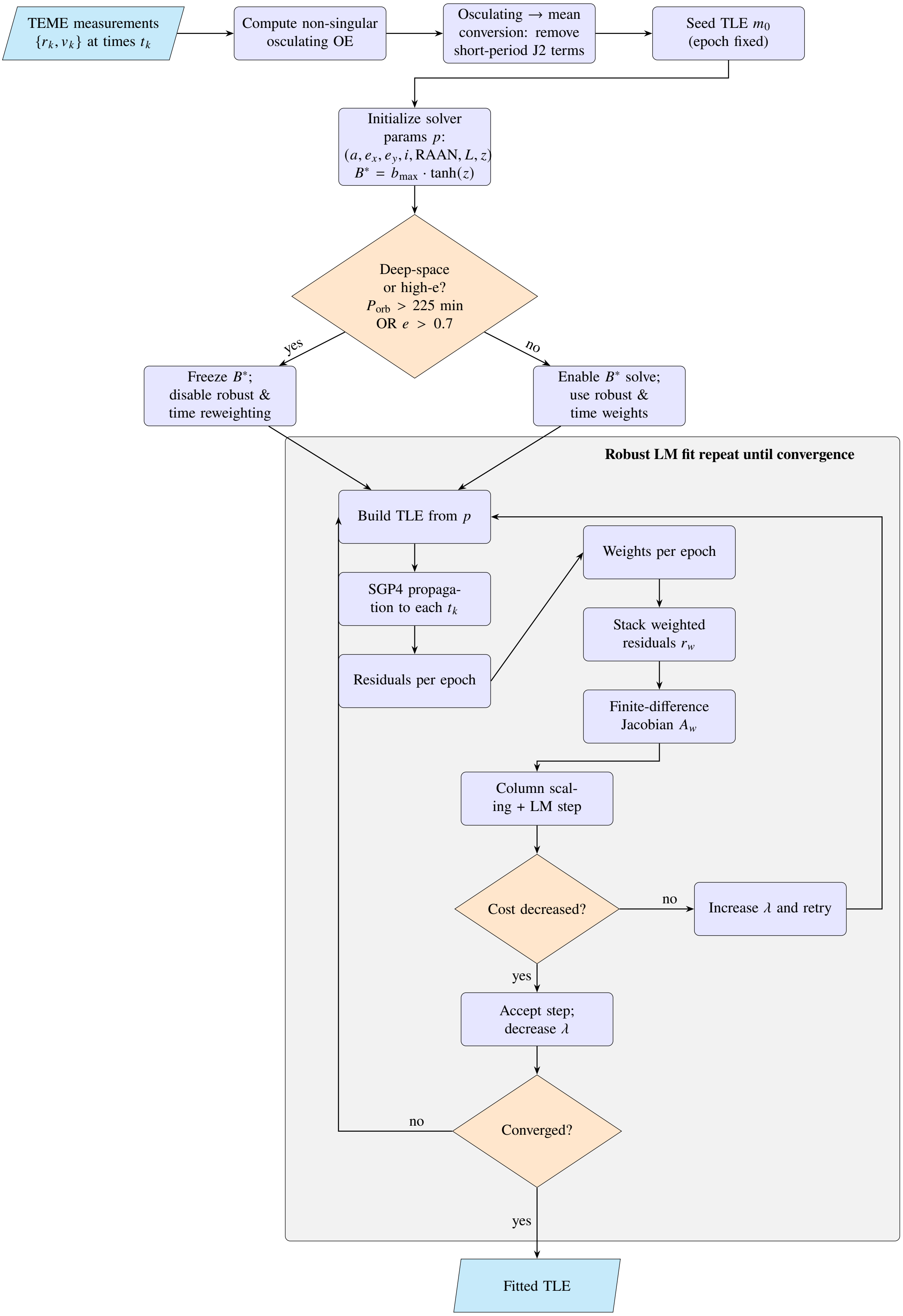

Fig. 7 Flowchart for Robust Pseudo-TLE Generation from GNSS Observations

References

[1] Ghasem Sharifi, Andrés Rabuñal-Gayo, Diego Navarro-Tapia, and Andrés Marcos. Development of an attitude determination and control strategy for the st3llarsat1 cubesat mission. In *Proc. SPIE 13546, Small Satellites Systems and Services Symposium (4S 2024)*, volume 13546, page 1354629. SPIE, Mar. 2025. doi: 10.1117/12.3061928, `https://doi.org/10.1117/12.3061928`.

[2] Fernando Solano Almena, Andrés Infante, Verónica Sastre, and Andrés Marcos Esteban. Mission analysis of the st3llarsat1 “boira” 2u cubesat: from bdr to fdr. Poster, presented at the Small Satellites & Services International Forum (SSSIF’24), Málaga, Spain, 20–22 Feb 2024, 2024. Abstract or poster only; full text not available. `https://www.researchgate.net/publication/378652706_Mission_Analysis_of_the_ST3LLARsat1_BOIRA_2U_CubeSat_from_BDR_to_FDR?channel=doi&linkId=65e22fb2adc608480af50983&showFulltext=true`.

[3] J. C. S. Bennett, Jianjun Sang, Chris Smith, and Kefei Zhang. Improving low-earth orbit predictions using two-line element data with bias correction. In *Advanced Maui Optical and Space Surveillance Technologies Conference (AMOS)*, 2012.

[4] David A. Vallado and Paul Crawford. SGP4 orbit determination. In *Proceedings of the AIAA/AAS Astrodynamics Specialist Conference and Exhibit*, number AIAA 2008-6770, Honolulu, Hawaii, 2008. American Institute of Aeronautics and Astronautics (AIAA), American Institute of Aeronautics and Astronautics. Center for Space Standards and Innovation, Colorado Springs, CO, USA. `https://www.celestrak.org/publications/AIAA/2008-6770/`.

[5] Dirk Brouwer. Solution of the problem of artificial satellite theory without drag. Technical Report AFCRC-TN-59-638, October 1959. Project Space Track, AD0240342, Approved for public release; distribution unlimited. `https://apps.dtic.mil/sti/pdfs/AD0240342.pdf`.

[6] Felix R. Hoots and Ronald L. Roehrich. Models for propagation of norad element sets. Technical Report Spacetrack Report No. 3, Aerospace Defense Center, Office of Astrodynamics, Peterson Air Force Base, Colorado, USA, December 1980. Approved for public release; distribution unlimited. Package compiled by T. S. Kelso (1988). `https://celestrak.org/publications/AIAA/1980-657`.

[7] David A. Vallado, Paul Crawford, Richard Hujsak, and T. S. Kelso. Revisiting spacetrack report #3: Rev 2. In *AIAA/AAS Astrodynamics Specialist Conference*, Keystone, Colorado, USA, August 2006. American Institute of Aeronautics and Astronautics. AIAA Paper 2006-6753, Revision 2. doi: 10.2514/6.2006-6753, `https://www.researchgate.net/publication/268555947_Revisiting_Spacetrack_Report_3`.

[8] Anthony Holincheck and Janet Cathell. Improved orbital predictions using pseudo observations: Maximizing the utility of SGP4-XP. In *Advanced Maui Optical and Space Surveillance Technologies Conference (AMOS)*, 2021.

[9] Dave Conkey and Mitchell Zielinski. Assessing performance characteristics of the SGP4-XP propagation algorithm. In *Advanced Maui Optical and Space Surveillance Technologies Conference (AMOS)*, 2022.

[10] Creon Levit and William Marshall. Improved orbit predictions using two-line elements. *Advances in Space Research*, 47(7):1107–1115, 2011.

[11] Junyu Chen and Chusen Lin. Research on enhanced orbit prediction techniques utilizing multiple sets of two-line element. *Aerospace*, 10(6):532, 2023. doi: 10.3390/aerospace10060532.

[12] Jinghong Liu, Wanting Long, Yunchen Wu, Jin Xu, Jizhang Sang, and Xiangxu Lei. TLE orbit determination using simplex method. *Geodesy and Geodynamics*, 14(5):438–455, 2023. doi:10.1016/j.geog.2023.03.004.

[13] Jake Gunther, Todd K. Moon, and Charles Swenson. Orbit refinement for doppler removal using observations from multiple frequencies, multiple ground sites, and multiple overpasses. In *Advanced Maui Optical and Space Surveillance Technologies Conference (AMOS)*, 2022.

[14] Y. Li, Z. Wang, and P. Gong. LSTM-based drag coefficient estimation for accurate LEO orbit propagation. *Journal of Spacecraft and Rockets*, 62(2):345–357, 2025.

[15] M. Rahman, S. Hudson, and J. Knapp. Machine learning corrections to SGP4 for improved conjunction assessment. *IEEE Transactions on Aerospace and Electronic Systems*, 60(1):93–104, 2024.

[16] Giacomo Acciarini, Atılım Güneş Baydin, and Dario Izzo. Closing the gap between SGP4 and high-precision propagation via differentiable programming, 2024. arXiv preprint.

[17] ESA Space Debris Mitigation Working Group. Esa space debris mitigation requirements. Technical Report ESSB-ST-U-007, European Space Agency (ESA), October 2023. ESA UNCLASSIFIED – For Official Use.

[18] David A. Vallado. *Fundamentals of Astrodynamics and Applications*. Microcosm Press, Hawthorne, CA, 4th edition, 2013. ISBN: 978-1881883180.

[19] Oliver Montenbruck and Eberhard Gill. *Satellite Orbits: Models, Methods, and Applications*. Springer, 2000.

[20] M. J. H. Walker, L. Ireland, and J. Owens. A set of modified equinoctial orbital elements. *Celestial Mechanics*, 36:409–419, 1985.

[21] R. H. Lyddane. Small eccentricities and inclinations in the brouwer theory of the artificial satellite. *The Astronomical Journal*, 68:555–558, 1963.

[22] Yuval Tassa, Nicolas Mansard, and Emo Todorov. Control-limited differential dynamic programming. In *Proceedings of the IEEE International Conference on Robotics and Automation (ICRA)*, pages 1168–1175, Hong Kong, China, 2014. IEEE. doi: 10.1109/ICRA.2014.6907001, `https://ieeexplore.ieee.org/document/6907001`.

[23] Alessio Farcomeni and Laura Ventura. An overview of robust methods in medical research. Working Paper Series 2, Department of Statistical Sciences, University of Padua, Mar. 2010. Working Paper Series No. 2.

[24] Peter J. Huber. *Robust Statistics*. Wiley, New York, 1981.

[25] Paul W. Holland and Roy E. Welsch. Robust regression using iteratively reweighted least-squares. *Communications in Statistics - Theory and Methods*, 6(9):813–827, 1977. doi: 10.1080/03610927708827533.

[26] Space-Track. Space-track satellite catalog and space situational awareness data, 2025. Accessed: 2025-10-22. `https://www.space-track.org/`.

[27] SkyTraq Technology Inc. Orion b16 high performance 11 quad constellation gnss receiver module for low earth orbit application. Product Datasheet, 2022. Revision 1.5.

[28] Kathleen Riesing and Kerri Cahoy. Two line element sets of cubesats in leo: Accuracy assessment and estimation techniques for improvement. In *Proceedings of the 29th Annual AIAA/USU Conference on Small Satellites*, Logan, Utah, USA, 2015. AIAA/USU. Faculty Advisor: Kerri Cahoy, Massachusetts Institute of Technology. `https://www.researchgate.net/publication/268469614_Propagation_of_CubeSats_in_LEO_using_NORAD_two_line_element_sets_Accuracy_and_update_frequency`.